15
Strain-Induced Nonlinear Optics in Silicon

Clemens Schriever, Christian Bohley, and Ralf B. Wehrspohn

15.1
Introduction

In contrast to ordinary linear optics where the modification of light by the presence of an optical material system is investigated, in nonlinear optics the focus lies on the modification of the optical properties of a material system by the presence of light. Because only laser light is intense enough to stimulate such processes, the development of the first laser by Maiman [1] in 1960 also initiated the research in the field of nonlinear optics, leading to the discovery of second harmonic generation (SHG) in 1961 by Franken *et al.* [2]. After the first steps in the sixties and early seventies [3–6] and a phase of low activity in the eighties, there has been much progress in nonlinear optics in the past 10 years with the focus on investigation techniques for solid state physics. Especially, in integrated optics materials, nonlinear optical properties have been exploited to create fast optical switches and modulators.

In the field of material diagnosis, the effect of second harmonic generation has turned out to be a sensitive tool for the investigation of surfaces and interfaces in optical transparent systems. Its strong dependence on structural symmetry makes this technique a suitable tool for the investigation of lattice strains that affect the symmetry of the material. In this section, the effect of SHG and its capabilities for the investigation of strains in silicon will be elucidated. In Section 15.2, a short introduction to the fundamentals of SHG is given followed by a more detailed description of its relation to structural symmetry in Section 15.3. Different sources of radiation at the second harmonic frequency are specified and the azimuthal SHG intensity distribution for bulk and surface SHG is deduced for the cases of (111)- and (100)-oriented silicon. In Section 15.4, the modification of the SHG signal due to the strain-induced lattice deformation is investigated. Section 15.5 gives an overview of recent developments in the field of integrated optics that apply strain-induced linear and nonlinear optical effects.

Mechanical Stress on the Nanoscale: Simulation, Material Systems and Characterization Techniques, First Edition. Edited by Margrit Hanbücken, Pierre Müller, and Ralf B. Wehrspohn.

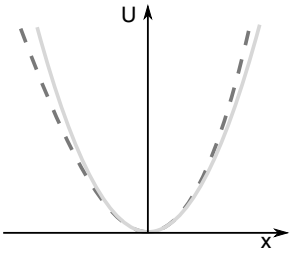

Figure 15.1 Potential energy function of a noncentrosymmetric medium (dashed line) in comparison to the symmetric potential energy function of a centrosymmetric medium (solid line).

15.2
Fundamentals of Second Harmonic Generation in Nonlinear Optical Materials

Second harmonic generation describes the case of nonlinear light–matter interaction, which is based on the second-order nonlinear susceptibility $\chi^{(2)}$. The reason for this effect originates from the fact that for high excitation intensities, the excited electrons cannot be approximated as linear oscillators following Hooke's law. Because of their large displacement around the equilibrium position, the electronic potentials of neighboring atoms have to be considered as well. Thus, the next higher order term of the restoring force has to be taken into account:

$$F_{\text{rest}} = -k^{(1)}x - k^{(2)}x^2 \tag{15.1}$$

This leads to a corresponding potential energy function:

$$U = \frac{1}{2}m\omega_0^2 x^2 + \frac{1}{3}m\delta x^3 \tag{15.2}$$

As shown in Figure 15.1, the resulting potential has to be asymmetric for second-order nonlinear contributions and it can, therefore, exist only in media that do not show inversion symmetry. In all other cases, $\delta = 0$ in Eq. (15.2).[1)] For the induced polarization, this leads to an additional term that depends quadratically on the incident electric field:

$$\vec{P}^{(\text{NL})}(t) = \chi^{(1)}\vec{E}(t) + \chi^{(2)}\vec{E}^2(t) \tag{15.3}$$

Considering an exciting laser beam with an electric field,

$$\vec{E}(t) = E\mathrm{e}^{-i\omega t} + \text{c.c.} \tag{15.4}$$

1) This can be proven by a simple consideration. Assume a given nonlinear polarization $P(t) = \chi^{(2)}E(t)^2$ for the electric field $E(t)$. Changing the sign of the applied electric field, the induced polarization has to change to $-P(t) = \chi^{(2)}[-E(t)]^2$ because of the inversion symmetry of the medium. Both equations together are valid only for $\chi^{(2)} = 0$.

the second-order term $\vec{P}^{(2)}(t)$ takes the form

$$\vec{P}^{(2)}(t) = 2\chi^{(2)}EE^* + \left(\chi^{(2)}E^2 e^{-i2\omega t} + \text{c.c.}\right) \tag{15.5}$$

The first term of the second-order polarization is independent of frequency and leads to a static electric field. This effect is known as optical rectification. The second term shows a dependence on the frequency 2ω. This is the second harmonic term of the induced nonlinear polarization. If we put Eq. (15.3) in combination with Eq. (15.5) into the inhomogeneous wave equation for linear optical interaction, we obtain the wave equation for nonlinear optical media [7]:

$$\nabla^2\vec{E} - \frac{n_\omega^2}{c^2}\frac{\partial^2\vec{E}}{\partial t^2} = \frac{\partial^2\vec{P}^{(\text{NL})}}{\partial t^2} \tag{15.6}$$

where n_ω is the refraction index and c is the speed of light in vacuum. For the polarization $\vec{P}^{(2)}(t)$ in Eq. (15.5), the solution of Eq. (15.6) is an electric field that oscillates at the second harmonic frequency of the exciting radiation. It is important to note that Eq. (15.6) is now a *nonlinear* partial differential equation because of the quadratic dependence on the electric field induced by the polarization. As a consequence, solutions of this equation cannot be derived by linear combination of known solutions.

This process can be regarded as an exchange of photons with different frequency components, whereas two photons with frequency ω are annihilated and simultaneously one photon with the frequency of 2ω is generated, as it is depicted in Figure 15.2. During this process, an electron absorbs a first photon and is lifted from the ground state to a virtual state. Because of the high intensity of the exciting beam, it can absorb an additional photon before it relaxes into the ground state. From this higher virtual state, it decays among the emission of a photon, which has twice the energy of the absorbed ones.

This process is not limited to the case of equal excitation frequencies. For different frequencies, additional processes like sum-frequency generation are possible. Here, two photons at ω_1 and ω_2 are absorbed and one photon at frequency $\omega_3 = \omega_1 + \omega_2$ is generated. It is also possible to generate light at lower frequency ω_3 by difference-frequency generation. In this case, the nonlinear interaction leads to the generation of a photon at $\omega_3 = \omega_1 - \omega_2$. However, this is beyond the scope of this chapter, additional information may be found in Ref. [7].

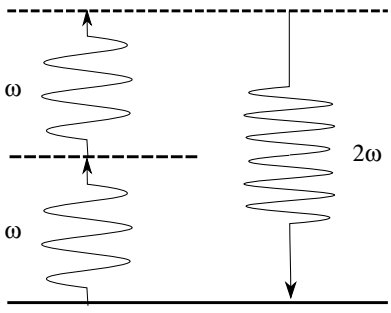

Figure 15.2 Second harmonic generation regarded as annihilation of two photons at frequency ω and simultaneous generation of one photon at frequency 2ω.

It is important to note that the nonlinear susceptibility $\chi^{(2)}$ in Eq. (15.3) has a high sensitivity to structural properties and, therefore, cannot be simplified to a scalar, like it can be done in the case of the linear susceptibility of an isotropic medium. In its general form, $\chi^{(2)}$ is a third rank tensor with 27 independent components, leading to the polarization components:

$$P_i(2\omega) = \sum_{jk} \chi^{(2)}_{ijk}(2\omega, \omega) E_j(\omega) E_k(\omega) \tag{15.7}$$

where $i, j, k = x, y, z$. However, the treatment of this tensor can often be simplified. Many of the tensor components are equal to each other because the indices j and k can be interchanged in the case of SHG. This allows to use a contracted notation known as Kleinman notation [7]. Here, the indices j, k are replaced by a single index l according to the following prescription:

jk	11	22	33	23,32	31,13	12,21
l	1	2	3	4	5	6

The tensor is thereby reduced to 18 independent components. In this notation, the nonlinear polarization responsible for SHG can be written in the form of a matrix equation:

$$\begin{bmatrix} P_x(2\omega) \\ P_y(2\omega) \\ P_z(2\omega) \end{bmatrix} = \begin{bmatrix} d_{11} & d_{12} & d_{13} & d_{14} & d_{15} & d_{16} \\ d_{21} & d_{22} & d_{23} & d_{24} & d_{25} & d_{26} \\ d_{31} & d_{32} & d_{33} & d_{34} & d_{35} & d_{36} \end{bmatrix} \begin{bmatrix} E_x(\omega)^2 \\ E_y(\omega)^2 \\ E_z(\omega)^2 \\ 2E_y(\omega)E_z(\omega) \\ 2E_x(\omega)E_z(\omega) \\ 2E_x(\omega)E_y(\omega) \end{bmatrix} \tag{15.8}$$

Furthermore, many of the $\chi^{(2)}_{ijk}$ components will vanish or become equal to each other because of the structural symmetry of the investigated material. To identify these components, the symmetry group of the considered material has to be specified. Each symmetry group contains transformations that leave the lattice structure unaffected. Because of its relation to the materials structural properties, the $\chi^{(2)}_{ijk}$ tensor is also invariant under these transformations. By the application of the symmetry operators, the tensor elements that have to be equal to zero to guarantee the invariance can be determined [8].

15.3 Second Harmonic Generation and Its Relation to Structural Symmetry

In this section, the influence of certain structural symmetries on the components of the second-order nonlinear susceptibility in Eq. (15.8) is investigated besides the origin of the SHG signal in silicon.

15.3.1
Sources of Second Harmonic Signals

Generally, the sources of second harmonic generation can be separated into two parts: the second harmonic signal that is generated in the bulk of the excited material and the signal generated at the interface between the material and the adjacent medium. Comparing both contributions in the case of a noncentrosymmetric medium shows that the contribution of the bulk signal is much larger than that of the signal from the surface [9]. Because the contributing bulk volume is much larger than the volume that can be regarded as the surface, the investigation of SHG from surfaces and interfaces is limited to the case of centrosymmetric media where the dipolar bulk contribution vanishes. For this case, Guyot-Sionnest and Shen [9] have shown that bulk and interface contribution can be on the same order of magnitude. For media with high dielectric contrast, they predict that the interface contribution should actually dominate the second harmonic signal. This is valid for reconstructed surfaces in vacuum [10]; however, for silicon with a native oxide, the contribution of bulk and surface are reported to be comparable [11].

In the case of silicon, bulk and surface contribution may have different sources [9, 12, 13]. Because the surface shows no inversion symmetry, there is a dipolar contribution to the second harmonic signal:

$$P^{\mathrm{s,dp}}(2\omega) = \chi^{\mathrm{s,dp}}_{ijk} E_j(\omega) E_k(\omega) \tag{15.9}$$

In addition, there is a quadrupolar contribution that originates from a surface layer with thickness $d \ll \lambda$ because of the discontinuity of the electric field normal component [12, 13]:

$$P^{\mathrm{s,qp}}(2\omega) = \chi^{\mathrm{s,qp}}_{ijzz} E_j(\omega) \nabla_z E_z(\omega) \tag{15.10}$$

Because the bulk silicon is centrosymmetric, only higher order quadrupolar contributions to the second harmonic signal can occur. They can be described with a fourth rank tensor of the form

$$P^{\mathrm{b,qp}}_i(2\omega) = \Gamma_{ijkl} E_j(\omega) \nabla_k E_l(\omega) \tag{15.11}$$

In the case of cubic bulk symmetry, Eq. (15.11) is usually expressed by the use of phenomenological constants $\delta, \beta, \gamma, \zeta$ in the form [6, 9, 11, 14]

$$P^{\mathrm{b,qp}}_i(2\omega) = (\delta - \beta - 2\gamma)(\vec{E}\nabla)E_i + \beta E_i(\nabla \cdot \vec{E}) + \gamma \nabla_i(\vec{E} \cdot \vec{E}) + \zeta E_i \nabla_i E_i \tag{15.12}$$

For SHG in a homogeneous medium excited by a transverse plane wave, the first two terms are equal to zero. A detailed description can be found in Ref. [6]. In the case

of SHG in reflection, the third term gives an isotropic contribution. This term and the anisotropic fourth term will be considered in detail later.

If there is an additional inhomogeneous strain applied to the silicon, for example, by the oxidation of the silicon surface, a further source of SHG can occur. The emerging biaxial strains lift the centrosymmetry of the bulk material in the vicinity of the interface, giving rise to a dipolar second harmonic contribution. Because the strain translates the surface symmetry into the bulk material, the generated second harmonic signal shows the same symmetry as the dipolar contribution of the surface [13, 15–17]:

$$P_{\mathrm{str}}^{\mathrm{dp}}(2\omega) = \chi_{ijk}^{(2)\mathrm{dp,str}}(z) E_j(\omega) E_k(\omega) \tag{15.13}$$

This effect will be discussed in detail in Section 15.4.

Furthermore, in connection with the oxidation of silicon, the effect of a static electric field-induced second harmonic (EFISH) can occur. In this case, an additional static electric field, breaking the inversion symmetry, enhances the dipolar second harmonic signal:

$$P_{\mathrm{EFISH}}^{\mathrm{dp}}(2\omega) = \chi_{ijkz}^{(3)\mathrm{dp}} E_j(\omega) E_k(\omega) \vec{E}_0 \tag{15.14}$$

The static field originates from a space–charge region at the interface that can occur during oxidation. For certain process and substrate parameters, the static electric field is believed to be strong enough to lift the symmetry along the normal direction [18].

15.3.2
Bulk Contribution to Second Harmonic Generation

To derive an expression for the phenomenological dependence of the SHG intensity on the structural symmetry of the investigated material, it is convenient to treat bulk and surface contribution separately. It is clear from Eq. (15.12) that the induced nonlinear bulk polarization can be expressed as

$$P_i^{(2\omega)} = \gamma \nabla_i (\vec{E} \cdot \vec{E}) + \zeta E_i \nabla_i E_i \tag{15.15}$$

where the first term shows isotropic behavior and the last term an anisotropic dependence on the crystal orientation. As exciting beam we consider a single plane wave at frequency ω that penetrates into the medium with a dielectric constant $\varepsilon(\omega)$ at an angle θ_0, as shown in Figure 15.3. Its electric field has the form

$$\vec{E}_0(\vec{r}, t) = \vec{E}_0 \mathrm{e}^{i(\vec{k} \cdot \vec{r} - \omega t)} \tag{15.16}$$

The electric field amplitude can be written as a superposition of s- and p-polarized components:

$$\vec{E}_0 = E_{0,\mathrm{p}} \hat{p} + E_{0,\mathrm{s}} \hat{s} \tag{15.17}$$

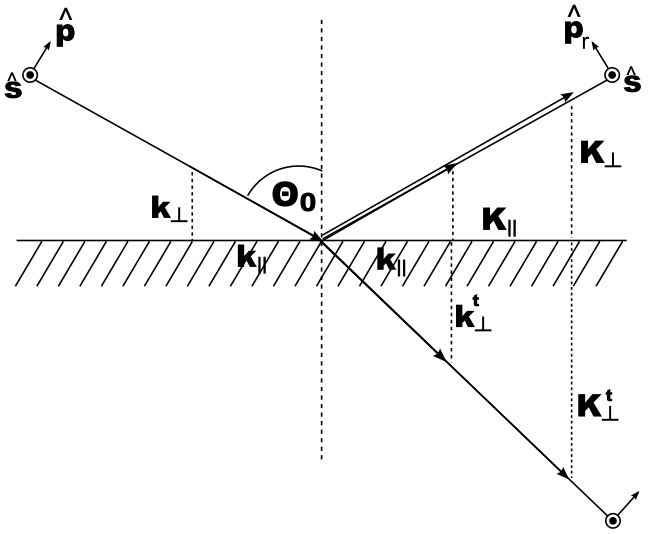

Figure 15.3 Schematic drawing of SHG in reflection. The respective waves can be regarded as consisting of vector components parallel ($k_{||}$) and normal ($k_{\perp}$) to the sample surface. k denotes a wave vector at fundamental, while K denotes a wave vector at second harmonic frequency. The normal components scale with the refractive index of the respective medium and frequency.

It is convenient to describe the propagation of the incident beam in a beam coordinate system with the axes $\hat{s}, \hat{k}_{||}$, and $\hat{z}$, whereas $\hat{z}$ is normal and $\hat{k}_{||}$ is parallel to the sample surface. Thus, the two polarization directions are

$$\hat{s} = \hat{k}_{||} \times \hat{z} \quad \text{and} \quad \hat{p} = \frac{k_{||}\hat{z} + k_{\perp}\hat{k}_{||}}{\omega/c} \tag{15.18}$$

As for the incident beam, it is convenient to define a coordinate system for the investigated medium. Its axes $(\hat{x}', \hat{y}', \hat{z}')$ are chosen to have the z-axis perpendicular to the respective crystal face. Thus, for the different crystal faces, the coordinates related to the particular standard crystal axes $(\hat{x}, \hat{y}, \hat{z})$ are transformed into the coordinates related to $(\hat{x}', \hat{y}', \hat{z}')$ by

$$\begin{pmatrix} x' \\ y' \\ z' \end{pmatrix} = \bar{D} \begin{pmatrix} x \\ y \\ z \end{pmatrix} \tag{15.19}$$

For (111)-oriented silicon, $\bar{D}$ takes the form

$$\bar{D}_{(111)} = \begin{pmatrix} \sqrt{2/3} & -1/\sqrt{6} & -1/\sqrt{6} \\ 0 & 1/\sqrt{2} & -1/\sqrt{2} \\ 1/\sqrt{3} & 1/\sqrt{3} & 1/\sqrt{3} \end{pmatrix} \tag{15.20}$$

For (100)-oriented silicon, the z-axis is just chosen to be perpendicular to the surface. With the z-axis defined equally in beam and crystal face coordinates, the residual coordinates can be transformed into each other by a simple rotation around the z-axis by an angle ϕ:

$$\begin{pmatrix} \hat{s} \\ \hat{k}_{||} \\ \hat{z} \end{pmatrix} = \begin{pmatrix} \sin(\phi) & -\cos(\phi) & 0 \\ \cos(\phi) & \sin(\phi) & 0 \\ 0 & 0 & 1 \end{pmatrix} \begin{pmatrix} \hat{x}' \\ \hat{y}' \\ \hat{z}' \end{pmatrix} \tag{15.21}$$

To investigate the second harmonic electric fields generated by the polarization in Eq. (15.15), it is useful to deal with the isotropic and anisotropic parts separately. The isotropic part remains unaffected by the coordinate transformation from crystal to beam coordinates. For the anisotropic part, the partial derivatives of the electric field

$$\vec{E}_{\mathrm{t}}(\vec{r},t) = \vec{E}_0 \mathrm{e}^{i(\vec{k}_t \cdot \vec{r} - \omega t)}, \quad \omega_{\mathrm{t}}^2 = \varepsilon(\omega)(\omega_0/c)^2 - k_{||}^2 \tag{15.22}$$

have to be solved first. With the derivatives in beam coordinates,

$$\nabla_s = 0, \quad \nabla_{k_{||}} = ik_{||}, \quad \nabla_z = -i\omega \tag{15.23}$$

the nonlinear polarization transformed into beam coordinates has the form

$$P_{i,\mathrm{anis}}^{(2\omega)} = i\omega/cn\zeta M'_{i\ln} E'_l E'_n \tag{15.24}$$

The elements $M'_{i\ln}$ correspond to the transformations from standard crystal axes to beam coordinates. Their expressions can be found in Sipe *et al.* [14].

Solving the nonlinear wave equation (Eq. (15.6)) in the medium for a polarization of the form

$$\vec{P}_{\mathrm{anis}}^{(2\omega)}(\vec{r},t) = \vec{P}^{(2\omega)}(z)\mathrm{e}^{i(2\vec{k}\cdot\vec{r}(x,y)-2\omega t)} + \mathrm{c.c.} \tag{15.25}$$

leads to an electric field outside the medium of the form

$$\vec{E}^{(2\omega)}(z) = \left(E_{\mathrm{s}}^{(2\omega)}\hat{s} + E_{\mathrm{p}}^{(2\omega)}\hat{p}_{\mathrm{r}}\right)\mathrm{e}^{iK_\perp z} \tag{15.26}$$

Further modification leads to the following relations between the incident electric fields and the generated SHG [14]. For (100)-oriented crystal faces, the second harmonic electric fields are as the following:

$$E_{\mathrm{s},s}^{(2\omega)} = K_{\mathrm{s}}\zeta b_{\mathrm{s},s}^{(100)} \sin(4\phi) E_{\mathrm{s}}^2 \tag{15.27}$$

$$E_{\mathrm{s},p}^{(2\omega)} = K_{\mathrm{s}}\zeta b_{\mathrm{s},p}^{(100)} \sin(4\phi) E_{\mathrm{p}}^2 \tag{15.28}$$

$$E_{\mathrm{p},p}^{(2\omega)} = K_{\mathrm{p}}\zeta\left(a_{\mathrm{p},p}^{(100)} + c_{\mathrm{p},p}^{(100)} \cos(4\phi)\right) E_{\mathrm{p}}^2 \tag{15.29}$$

$$E_{\mathrm{p},s}^{(2\omega)} = K_{\mathrm{p}}\zeta\left(a_{\mathrm{p},s}^{(100)} - c_{\mathrm{p},s}^{(100)} \cos(4\phi)\right) E_{\mathrm{s}}^2 \tag{15.30}$$

The coefficients $K_{s/p}$ depend on the angle of incidence θ_0, as well as the a, b, and c. The latter are determined by the components of the transformation tensor M'_{ijn} introduced in Eq. (15.24). M'_{ijn} also mediates the azimuthal dependence of the second harmonic electric field.

For (111)-oriented crystal faces, the second harmonic electric fields are deduced analogous to the (100)-oriented surfaces [14]:

$$E_{s,s}^{(2\omega)} = K_s \xi b_{s,s}^{(111)} \sin(3\phi) E_s^2 \tag{15.31}$$

$$E_{s,p}^{(2\omega)} = K_s \xi b_{s,p}^{(111)} \sin(3\phi) E_p^2 \tag{15.32}$$

$$E_{p,p}^{(2\omega)} = K_p \xi \left(a_{p,p}^{(111)} + c_{p,p}^{(111)} \cos(3\phi) \right) E_p^2 \tag{15.33}$$

$$E_{p,s}^{(2\omega)} = K_p \xi \left(a_{p,s}^{(111)} - c_{p,s}^{(111)} \cos(3\phi) \right) E_s^2 \tag{15.34}$$

The isotropic SHG electric fields originating from the first term of Eq. (15.15) can be derived similar to the anisotropic fields. This leads to the following:

$$E_{s,s}^{(2\omega)} = E_{s,p}^{(2\omega)} = 0 \tag{15.35}$$

$$E_{p,p}^{(2\omega)} = A\gamma E_p^2 \tag{15.36}$$

$$E_{p,s}^{(2\omega)} = A\gamma E_s^2 \tag{15.37}$$

Coefficient A depends on the angle of incidence θ_0. The isotropic contribution to the second harmonic signal is the same for all crystal orientations.

15.3.3
Surface Contribution to Second Harmonic Generation

In the next step, the SHG contribution from a silicon surface is investigated. Because the inversion symmetry of the bulk is lifted at the surface, a dipolar contribution can be observed. The contributing $\chi^{(2)}$ tensor components are determined by the crystal symmetry at the sample surface. Considering several surface layers for (111)-oriented silicon, a $C_{3,v}$ symmetry is obtained (see Figure 15.4). Because the $\chi^{(2)}$ tensor in Eq. (15.8) has to be unaffected by the application of the corresponding symmetry operators, many of its elements are zero or equal to other elements. This reduces the tensor to

$$\chi_{(111)}^{(2)} = \begin{pmatrix} d_{11} & -d_{11} & 0 & 0 & d_{15} & 0 \\ 0 & 0 & 0 & d_{15} & 0 & -d_{11} \\ d_{31} & d_{31} & d_{33} & 0 & 0 & 0 \end{pmatrix} \tag{15.38}$$

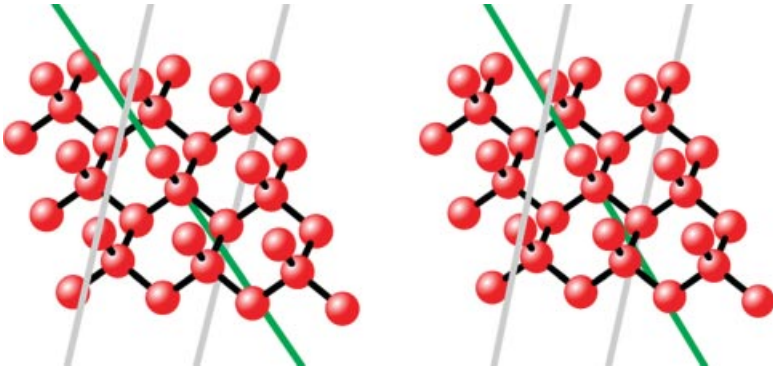

Figure 15.4 Stereo view of the silicon (111) face. The crystal shows threefold rotational symmetry, with the green axis as the rotation axis. The crystal also has planes of mirror symmetry. In the figure, one of these planes is indicated by two gray lines lying in this plane. The (111) face shows $C_{3,v}$ symmetry.[2)]

In the case of a (100)-oriented surface, the $\chi^{(2)}$ tensor has to be invariant under all operations of the group $C_{4,v}$. This reduces the tensor to

$$\chi^{(2)}_{(100)} = \begin{pmatrix} 0 & 0 & 0 & 0 & d_{15} & 0 \\ 0 & 0 & 0 & d_{15} & 0 & 0 \\ d_{31} & d_{31} & d_{33} & 0 & 0 & 0 \end{pmatrix} \tag{15.39}$$

As for derivation of the bulk second harmonic electric field, we also have to transform here the $\chi^{(2)}$ tensor from crystal coordinates $(\hat{x}, \hat{y}, \hat{z})$ to beam coordinates $(\hat{s}, \hat{k}_{||}, \hat{z})$. To calculate the surface second harmonic electric fields, an ansatz similar to Eq. (15.25) is used. In this case, the nonlinear polarization can be described as [19]

$$\vec{P}^{(2\omega)}(\vec{r}, t) = \vec{P}^{(2\omega)}_{\text{surf}} \delta(z - z_0) \left(e^{i(2\vec{k} \cdot \vec{r}(x,y) - 2\omega t)} + \text{c.c.} \right) \tag{15.40}$$

Here, we assume that the second harmonic field is generated in a thin surface layer of thickness z_0. δ is the function of Dirac.

Therefore, we obtain for a (111)-oriented silicon surface the s- and p-polarized second harmonic electric fields:

$$E^{(2\omega)}_{\text{s},s} = K_{\text{s}} b^{(111)}_{\text{s},s} d_{11} \sin(3\phi) E^2_{\text{s}} \tag{15.41}$$

$$E^{(2\omega)}_{\text{s},p} = K_{\text{s}} b^{(111)}_{\text{s},p} d_{11} \sin(3\phi) E^2_{\text{p}} \tag{15.42}$$

$$E^{(2\omega)}_{\text{p},p} = K_{\text{p}} \left(a^{(111)}_{1_{\text{p},p}} d_{31} + a^{(111)}_{2_{\text{p},p}} d_{15} + a^{(111)}_{3_{\text{p},p}} d_{33} + c^{(111)}_{\text{p},p} d_{11} \cos(3\phi) \right) E^2_{\text{p}} \tag{15.43}$$

2) Use the 3D free-viewing method that is called cross-eyed method. The eyes have to be aimed so that the lines of sight cross in front of the image.

$$E_{p,s}^{(2\omega)} = K_p\left(a_{p,s}^{(111)} d_{31} - c_{p,s}^{(111)} d_{11} \cos(3\phi)\right) E_s^2 \tag{15.44}$$

The s-polarized second harmonic signals show a sixfold rotational symmetry. The same symmetry can be exhibited by the p-polarized components; however, the signal mostly shows a threefold symmetry depending on the magnitude of the single tensor components. In the case of a (100)-oriented surface, the second harmonic fields are as the following:

$$E_{s,s}^{(2\omega)} = E_{s,p}^{(2\omega)} = 0 \tag{15.45}$$

$$E_{p,p}^{(2\omega)} = \left(a_{1_{p,p}}^{(100)} d_{31} + a_{2_{p,p}}^{(100)} d_{15} + a_{3_{p,p}}^{(100)} d_{33}\right) E_p^2 \tag{15.46}$$

$$E_{p,s}^{(2\omega)} = a_{1_{p,s}}^{(100)} E_s^2 \tag{15.47}$$

In this case, the surface SHG signal is isotropic. Nevertheless, the detected signal as superposition of bulk and surface contribution is anisotropic. Because of the similar symmetries of bulk and surface contribution, it is generally not possible to distinguish between both contributions unambiguously [9, 14, 20]. However, Bottomley *et al.* [21] proposed a theoretical solution for this problem by exploiting the fact that surface and bulk nonlinear susceptibilities are represented by tensors of different rank. This solution is applicable for (100) and (110) faces in the case that the phase of the SHG signal is known.

15.4
Strain-Induced Modification of Second-Order Nonlinear Susceptibility in Silicon

As explained in Section 15.2, for semiconductors with inversion symmetry, the second-order bulk nonlinearity does not exist in the electric dipole approximation, while a quadrupole-type nonlinearity can be observed. By this reason, the complete second harmonic signal is dominated by the surface dipole contribution that is rather weak.

In the late eighties, a new possibility to create an enhanced second harmonic signal caused by an electric dipole contribution from crystals with inversion symmetry was tested: an inhomogeneous deformation of the crystal lattice at the interface layer where the reflection occurs [16, 22, 23]. An increase in the second harmonic signal by more than two orders of magnitude caused by inhomogeneous mechanical stress was reported by Govorkov *et al.* [24]. A theory for this optical nonlinearity was first given in 1989 by Govorkov *et al.* for diamond-type crystals as Si and Ge [15, 24], later with a similar approach by Huang [17]. In these models, the sp^3 orbital concept is used, calculating the susceptibility tensor $\chi^{(2)}$ from the Hamiltonian of the covalent crystal bonds [25]. A phenomenological description using the concept of a strain-dependent photoelastic tensor as part of the dielectric permittivity tensor was presented some years later [26, 27].

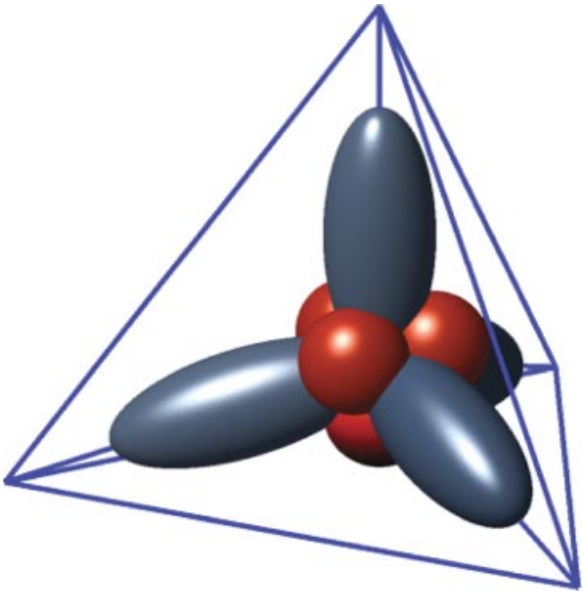

Figure 15.5 Tetrahedral geometry of hybrid orbitals of four silicon bonds in a silicon unit cell. The angle between two orbital axes is 109.5°. The nonlinear optical response of the whole cell corresponds to the geometric superposition of the nonlinear responses of each bond.

In the following, we will give an outline of the theory described by Govorkov *et al.* in Ref. [24] where the SHG susceptibility of the silicon layer is derived from dependence on the strain of the layer.

In the sp^3 orbital model (see Figure 15.5), a Hamiltonian considering the Coulomb interaction between the covalent bonds is defined. By introducing an additional term to the electron–phonon interaction, the Hamiltonian can be extended to the case of crystal deformation. Thus, it is possible to calculate complete orbitals as a superposition of the single wave functions. Expressions for the corresponding susceptibility tensor $\chi^{(2)}$ of the total bond Hamiltonians are derived with a model in Ref. [25].

Armstrong *et al.* showed that in a centrosymmetric material, SHG is forbidden in the electric dipole approximation (see also Section 15.2) [28]. An important condition for the violation of the centrosymmetry of a crystalline structure by strain is its inhomogeneity. This is guaranteed if the strain is induced by surface disturbances as mismatches or defects.

Assume a strain in a surface layer with a strain gradient in direction z normal to the interface. This can be, for example, due to the thermal oxidation of a thin layer onto the silicon substrate. If the strain is caused by structural mismatch in the presence of dislocations, the strain decreases exponentially with the substrate depth if the dislocations are at the substrate surface [29]. Thus, the strain is given by an atomic displacement vector $\vec{u}$ with

$$\operatorname{div} \vec{u} = \zeta_0 \exp(-\Gamma z) \tag{15.48}$$

where ζ_0 is the deformation value at the surface and Γ is the reciprocal of the deformation characteristic length with $\Gamma a \ll 1$, a being the bond length in the crystal. With the sp^3 model explained above, Govorkov *et al.* [24] stated that a stress-induced SHG signal I^{IH}, measured in reflection from a Si(001) interface, can be estimated with the material absorption α in cm^{-1} and I^Q as the bulk quadrupole SHG taken as a reference value. They found for weak absorption $\alpha(2\omega) \ll \Gamma$,

$$\frac{I^{IH}}{I^Q} = \left(4 \times 10^{-2} \alpha(2\omega)\zeta_0\right)^2 \tag{15.49}$$

and for strong absorption $\alpha(2\omega) \gg \Gamma$,

$$\frac{I^{IH}}{I^Q} = \left(4 \times 10^{-2} \Gamma\zeta_0\right)^2 \tag{15.50}$$

Hence, it can be concluded that for a slight variation of the deformation, the ratio of stress-induced and quadrupole SHG contribution is small. This could be confirmed in experiments where the deformation is created by thin films deposited upon the silicon substrate. Several groups of authors investigated SHG of silicon samples that are stressed with film layers grown upon the silicon surface by thermal oxidation. For the p-polarized SH components and a p-polarized probe beam at a Si(111) substrate with a 50 nm thick silicon oxide layer, Govorkov *et al.* achieved an SH intensity increase of a factor of 20 compared to the silicon substrate with native oxide. For silicide films (optically transparent Si_xNi_y polycrystalline layers) on Si(001), an SH increase of 200 was observed [24]. Huang investigated Si(111) substrates with thermally grown silicon oxide layers of different thickness [17]. According to Sipe *et al.* [14], the reflected SH signals have an azimuthal dependence of the form

$$I_{pp}^{IH} = \left|a_{pp} + c_{pp} \cos 3\phi\right|^2 I_p^2 \tag{15.51}$$

for a p-polarized SH signal of a p-polarized probe beam (cf. Eq. (15.33)) and

$$I_{ss}^{IH} = |b_{ss} \sin 3\phi|^2 I_s^2 \tag{15.52}$$

for the s-polarized SH signal of a s-polarized probe beam (cf. Eq. (15.31)). Here, a_{pp}, b_{ss}, and c_{pp} comprise the contributions from surface and bulk electric dipole and electric quadrupole terms. In Figure 15.6, the dependence of b_{ss} and c_{pp} on the thickness of the thermally grown silicon dioxide layer is shown. It can be assumed that the surface stress on the silicon substrate depends exponentially on the thickness of the silicon oxide layer that was grown thermally on it [30]. With a bulk stress σ,

$$\sigma = \sigma_0 \exp(-z/d) \tag{15.53}$$

depending exponentially on the depth z in the bulk (d is a decay length), for the tensor components of the inhomogeneous stress-induced second-order nonlinear susceptibility in dipole approximation holds after Ref. [15]:

$$\chi_{D,def}^{(2)} \propto \frac{\sigma_0}{d} \tag{15.54}$$

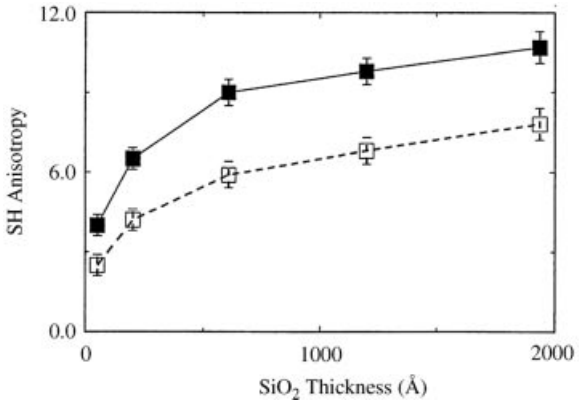

Figure 15.6 The cos 3ϕ respectively sin 3ϕ angular components c_{pp} (open squares) and b_{ss} (filled squares) of the azimuthal SH susceptibility in Eqs (15.51) and (15.52) versus the thickness of the silicon oxide layer on the Si (111) substrate. Reproduced from Ref. [17] with permission from the Japan Society of Applied Physics.

These considerations can explain that the angular components in Figure 15.6 depend exponentially on the silicon oxide layer thickness. The SH signal reflected from a Si(111) surface with silicon oxide layers of thicknesses between 5 and 60 nm was investigated by An [31] for different photon energies, revealing that the situation is more complex for thinner layers. This is explained with the influence of the interface layer between silicon and silicon oxide. For example, at a two-photon energy of 3.44 eV, the angular coefficients for the fourfold rotational anisotropies depend nonmonotonically on the silicon oxide layer thickness. It is to note that a thinner interface width corresponds to a larger oxide thickness if that is smaller than 50 nm [32].

Several authors investigated the SH signal from silicon with thermally oxidized layers for different frequencies of the input beam [31, 33, 34]. Daum *et al.* found a strong resonance band at 3.3 eV photon energy [33]. The resonance at 3.3 eV can be explained with the fact that the frequency dependence of the nonlinear susceptibility close to a resonance at the second harmonic frequency is approximately that of the linear susceptibility of the bulk material (see Figure 15.7). This linear susceptibility has a resonance at 3.37 eV, caused by the E_1 bandgap transitions in silicon. It is concluded that the resonance is enhanced by transitions between valence and conduction band states in a few monolayers at the interface between silicon and silicon oxide. Later, the difference between the nonlinear and linear resonance frequencies was explained as arising from interfering surface and bulk contributions that can distort the spectroscopic results taken for a single azimuthal angle [35]. Furthermore, An showed that the resonant photon energy value of 3.3 eV can slightly be influenced by the layer thickness if the layer is thinner than 100 nm [31].

Schriever *et al.* investigated a Si(111) SH signal with a fundamental wavelength of 800 nm in reflection (45°) depending on the strain of a silicon dioxide layer of a thickness between 10 and 250 nm Clemens Schriever, Christian Bohley, and Ralf B.

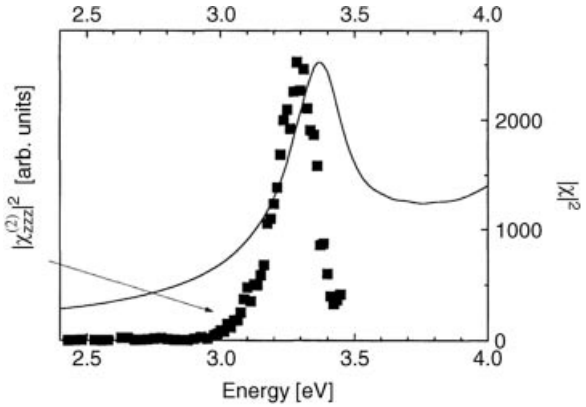

Figure 15.7 Spectral dependence of $|\chi^{(2)}_{zzz}|^2$ (filled symbols) evaluated from an oxidized Si (100) sample with an oxide layer thickness of 700 nm and of $|\chi|^2$ (solid line), with χ as linear bulk susceptibility of silicon, calculated from the dielectric function of Si with $\chi(2\omega) = \varepsilon(2\omega) - 1$. Reproduced with permission from Ref. [33]. Copyright American Physical Society.

Wehrspohn, "Strain dependence of second-harmonic generation in silicon", Optics Letters, Vol. 35, Issue 3, pp. 273-275 (2010). The p-polarized SH signal of a p-polarized probe beam, obeying Eq. (15.51) (cf. Eq. (15.33)), shows a linear dependence of the coefficients a_{pp} and c_{pp} on the layer strain (see Figure 15.8). This corresponds to the statement in Eq. (15.54), assuming that the second-order susceptibility induced by the silicon layer is proportional to the silicon interface stress. The linear relationship between susceptibility enhancement and strain could also be used in the reverse direction determining the stress level of a strained layer by analyzing the enhancement of the second harmonic generation. The average deviation of the measurements in Figure 15.8 is approximately 13%. For the reverse measurement of the stress level,

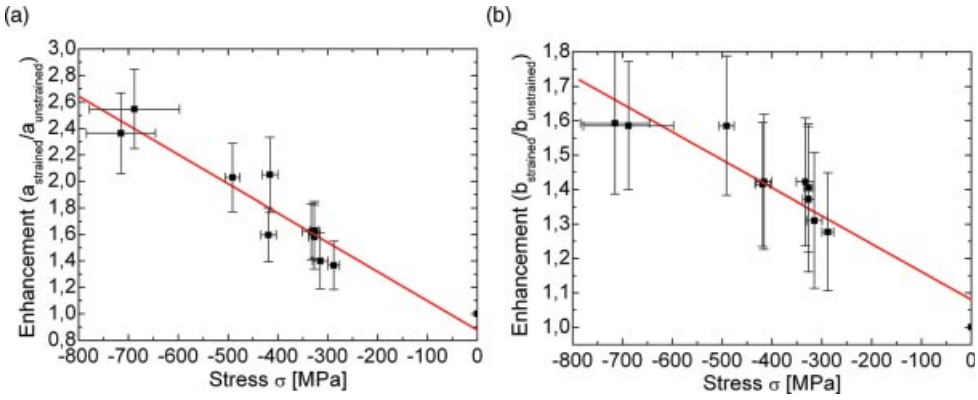

Figure 15.8 The angular components a_{pp} (a) and c_{pp} (b) of the azimuthal SH susceptibility in Eq. (15.51) versus the strain of the silicon oxide layer on the Si(111) substrate.

the same deviation is to be expected to occur because of the linear relation between both quantities. A considerable part of the deviation originates from the fact that the enhancement in Ref. Clemens Schriever, Christian Bohley, and Ralf B. Wehrspohn, "Strain dependence of second-harmonic generation in silicon", Optics Letters, Vol. 35, Issue 3, pp. 273-275 (2010) is measured relative to a single reference sample. Because different samples with slightly different substrate histories are compared, this enhances the error by approximately 6%. If SHG is used to investigate strained structures on one sample, the average error should be reduced below 7%. This method could also be used for high-resolution strain mapping, whereas the maximum resolution is limited to the half of the used wavelength due to Abbes resolution limit. However, because of its high sensitivity to structural symmetry, its main advantage compared to other methods would be the possibility to investigate the strain of buried interfaces situated between two centrosymmetric media.

Summarizing, detecting strain with the help of the enhancement of the SHG signal reflected by a silicon layer is in principle possible. It could be shown that for a known crystal orientation, the strain can be estimated by means of the linear dependence of the nonlinear signal on the strain Clemens Schriever, Christian Bohley, and Ralf B. Wehrspohn, "Strain dependence of second-harmonic generation in silicon", Optics Letters, Vol. 35, Issue 3, pp. 273-275 (2010).

15.5
Strained Silicon in Integrated Optics

Until now we were focused on the nonlinear optical properties arising from strained bulk silicon. However, in recent years, strained silicon has also found its way into the field of integrated optics. Similar to the field of microelectronics where it has proven itself as a viable material for transistors because of higher strain-induced charge mobilities [36], its advantages in integrated optics are now being explored. The linear and nonlinear properties could already be exploited, for example, in the design of a novel electro-optical modulator based on a strain-induced linear electro-optical effect [37, 38]. A further example that will be contemplated in this section is the strain-induced photoelastic effect. It leads to a strain-dependent shift of the refractive index and has been used to eliminate birefringence in ridge waveguides [39] or for electrically tunable phase matching processes in integrated optical devices [40, 41]. Using its nonlinear optical properties in combination with optimized photonic structures, strained silicon, similar to nonlinear organic polymers [42], could become a promising material candidate for the production of ultrafast all-optical computation devices.

15.5.1
Strain-Induced Electro-Optical Effect

The strain-induced electro-optical effect described by Jacobsen *et al.* [37] can be regarded as a special case of second harmonic generation. Instead of having two

electric fields of the form described in Eq. (15.4), here only one field is regarded, which means that the intensity of the incident light can be considered as low. For the second field, we have a strong static field $E_{\text{stat}}(\omega = 0)$ that is applied to the medium. For the second-order nonlinear polarization, we now get instead of Eq. (15.5)

$$\vec{P}^{(2)}(t) = \chi^{(2)}(\omega, \omega, 0)\vec{E}_{\text{stat}}(\vec{E}\mathrm{e}^{-i\omega t} + \text{c.c.}) \tag{15.55}$$

It is obvious that the nonlinear polarization describes a contribution to the polarization at the frequency of the incident field. Therefore, the prefactor $\chi^{(2)}(\omega, \omega, 0)\vec{E}_{\text{stat}}$ can be regarded as a nonlinear contribution to the refractive index:

$$n(E) = n_0 + \chi^{(2)} E_{\text{stat}} \tag{15.56}$$

This dependence of the refractive index on the applied electric field is known as the linear electro-optical or Pockels effect [7].

Jacobsen *et al.* [37, 38] used this effect to create an electro-optical modulator based on the principle of Mach-Zehnder interferometer (MZI) (Figure 15.9a). The MZI was etched into the silicon device layer of a silicon on insulator chip. To avoid optical coupling, they deposited 1.2 μm silicon dioxide on top of the device structure and additionally a highly strained silicon nitride layer on top of the sample to induce strain. By applying a static field to one of the arms of the MZI, the strain-induced susceptibility $\chi^{(2)}$ led to a change of the refractive index and thereby to a phase shift between the electric fields traveling through the respective arms. This effect was even enhanced by the use of photonic crystal structures (Figure 15.9b) whose parameters were chosen to result in a high effective group index n_g, thus slowing down the light considerably and enhancing the light–matter interaction (Figure 15.10). By shifting the phase of the electric fields, they presented their device as an optical switch showing transmission depending on the phase shift induced interference.

In addition, the device is compared with a $LiNbO_3$ modulator, thus determining the electro-optical coefficient of the strained silicon. For a slow light photonic crystal, they obtained a value of $\chi^{(2)}_{\text{eff}} \approx 830$ pm/V. However, the real value of the strained silicon is much smaller because it has to be scaled down by the effective group index to [37]

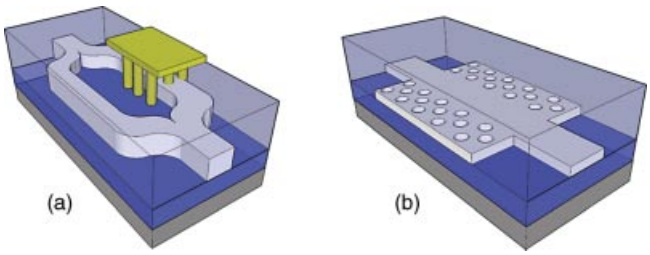

Figure 15.9 (a) Schematic drawing of a Mach-Zehnder interferometer (MZI) used in Ref. [37]. The incident beam is split into both arms of the MZI. The phase in one arm is modulated by a static electric field (yellow). (b) Showing that this effect can be enhanced if the light is slowed down by the presence of suitable photonic crystal structures.

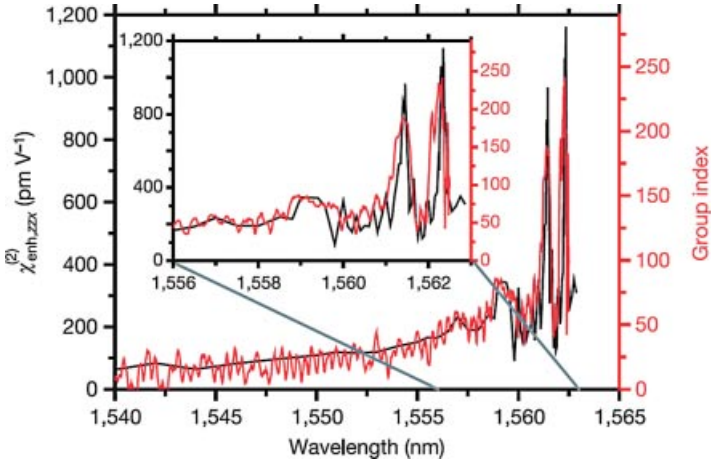

Figure 15.10 Comparison between the nonlinear coefficient $\chi^{(2)}_{enh}$ (black) and the group index n_g (red). $\chi^{(2)}_{enh}$ scales linearly with n_g that is determined by the parameters of the photonic crystal. Reproduced from Ref. [37] with permission from the Nature Publishing Group.

$$\chi^{(2)} = \frac{n}{n_g}\chi^{(2)}_{enh} = 15\ \text{pm/V} \tag{15.57}$$

Although this value is much smaller than the susceptibility of highly nonlinear materials like $LiNbO_3$ ($\chi^{(2)} \approx 360$ pm/V) [37], it has been shown in this work that the combination of strained silicon and proper optical design can compete with the established nonlinear materials.

15.5.2
Strain-Induced Photoelastic Effect

Contrary to the effects already described, the photoelastic effect used by Xu *et al.* [39] and Tsia *et al.* [40, 41] is a *linear* optical effect that is directly caused by strain. It describes the influence of strains on the refractive index tensor in an birefringent medium. The presence of strain leads to a linear dependence of the refractive index components on the symmetry of the single-strain tensor components, which results in [43]

$$n_{ij}(\sigma_{kl}) = n_{ij}(0) + \sum_{kl} C_{ijkl}\sigma_{kl} \tag{15.58}$$

Here, C_{ijkl} is the photoelastic tensor that depends on structural symmetries of the medium and on the applied strain field. The photoelastic effect can be depicted as a mechanical effect where the lattice spacing of the medium is changed by the applied strain in a certain direction. The process of light passing the medium can be regarded as a nonresonant absorption and reemission of photons at different atoms, which leads to a slower propagation in the medium described by the refractive index. If the

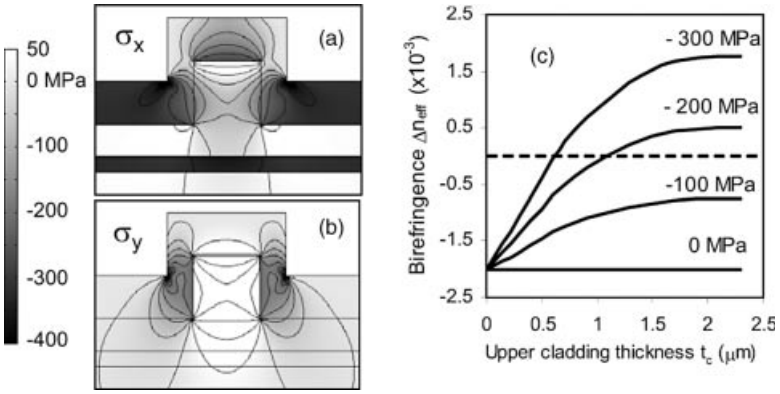

Figure 15.11 Calculated stress distribution in an SOI waveguide in (a) *x*-direction and (b) *y*-direction. (c) Showing the stress and thickness dependence of the birefringence. It saturates at a thickness of 2.5 μm because the stress in a thicker layer does not reach the waveguide anymore. Reproduced from Ref. [39] with courtesy of the Optical Society of America.

lattice is now spread in one direction, it is obvious that the speed of the propagating light is direction dependent.

The reverse effect is used by Xu *et al.* [39] for compensation of the geometry-induced birefringence in a ridge waveguide by the deposition of a straining layer. This induced birefringence originates from asymmetric conditions of the surrounding material (e.g., air on top, silicon oxide at the bottom) and from geometric deviations in the production process. The biaxial strain in the deposited layer also evokes strains in *x*- and *y*-directions in the core of the waveguide structure (Figure 15.11a and b). For a film with a thickness of 370 nm and a stress level of $\sigma = -320$ MPa, significant core stress contributions of $\sigma_x \approx -70$ MPa and $\sigma_y \approx -180$ MPa were calculated [39]. This stress anisotropy induces the birefringence that is used to compensate the birefringence originating from the geometry. Besides the tuning of the core stress by changing the external stress level, they also investigated the effect of increasing the cladding thickness, which also enhances the birefringence due to additional core stress (Figure 15.11c). Because the film stress is very sensible to deposition conditions, the variation of the cladding thickness might be more suitable for a fine-tuning of the birefringence. The effect on the refractive index can be significant as for a 2 μm thick oxide layer with $\sigma_{\text{film}} = -300$ MPa, an index change of $\Delta n = 1.6 \times 10^{-3}$ is calculated.

A similar approach is chosen by Tsia *et al.* [41], however, they take the idea one step further by creating a waveguide with electrical tunable birefringence. Therefore, they cover their ridge waveguides with a transparent layer of 500 nm silicon oxide to avoid absorption losses by the piezoelectric manipulator, which is put on the top. The strain applied by this device can thus be varied by changing the applied voltage (Figure 15.12). The induced stress is much smaller than the stress from the cladding layer, the calculated core stress level induced solely by the piezo is $\sigma_x^{\text{piezo}} = -1$ MPa and $\sigma_y^{\text{piezo}} = 12$ MPa, respectively. However, this results in an induced birefringence

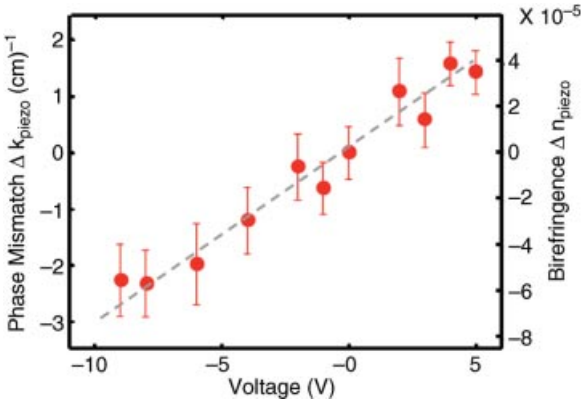

Figure 15.12 Dependence of phase mismatch and birefringence of an SOI waveguide on the voltage applied to the piezoelectric manipulator. Reproduced from Ref. [40] with courtesy of the Optical Society of America.

of $\Delta n \approx 3 \times 10^{-4}$. This effect is believed to be sufficient to correct structural deviations in waveguide dimensions of approximately 50 nm.

In Ref. [40], Tsia *et al.* used the electrical tunability of the refractive index to achieve phase matching between different light waves in a coherent anti-Stokes Raman scattering (CARS) experiment. It is reported that the conversion efficiency can be enhanced by 5–6 dB with the variation of the applied piezoelectricity.

The idea of achieving phase matching by strain modification is fascinating for the case that phase matching capabilities are used to investigate strain-induced nonlinear processes itself like SHG in silicon waveguides. Because the fundamental (ω) and second harmonic (2ω) waves will generally propagate at different velocities due to refractive index dispersion, phase matching is crucial to avoid destructive interference between the different waves. This could be achieved by tuning the directional refractive indices by applying suitable strain to the waveguide.

15.6 Conclusions

The recognition of the possibility to alter material properties by the application of strain and the progress made in nonlinear optics led to efforts to investigate silicon as the most important semiconductor material concerning these aspects. The origin of the nonlinear response arising from the strained silicon could be described theoretically. This theory gives the starting point for the modification of the second-order nonlinear properties of silicon in a determined manner. It could be compared with experimental results that verify the relationship between strain and the $\chi^{(2)}$ susceptibility. It was shown that the second harmonic signal can be drastically enhanced by applying strain to a silicon substrate, for instance, by a thermally grown silicon oxide

layer. Thus, SHG with its high sensitivity to interfaces is a suitable method to investigate strains induced at material interfaces.

Until now, the direct SHG although seems to be suited rather for analyzing techniques, other strain-induced effects have been implemented in integrated optical devices. For example, a Mach-Zehnder interferometer using the linear electro-optical effect in a strained silicon photonic crystal has been used as an electro-optical modulator. The use of strained silicon in combination with suitable photonic design can open the possibility to create affordable nonlinear optical devices with features that can compete with properties of conventional nonlinear materials. First obstacles like the dynamic control of strain by the use of the piezoelectric effect have already been overcome.

References

1 Maiman, T.H. (1960) Stimulated optical radiation in ruby. *Nature*, **187**, 493–494.

2 Franken, P.A., Hill, A.E., Peters, C.W., and Weinreich, G. (1961) Generation of optical harmonics. *Phys. Rev. Lett.*, **7**, 118–119.

3 Bloembergen, N. and Pershan, P.S. (1962) Light waves at the boundary of nonlinear media. *Phys. Rev.*, **128**, 606–622.

4 Kleinman, D.A. (1962) Theory of second harmonic generation of light. *Phys. Rev.*, **128**, 1761–1775.

5 Terhune, R.W., Maker, P.D., and Savage, C.M. (1962) Optical harmonic generation in calcite. *Phys. Rev.*, **8**, 404–406.

6 Bloembergen, N., Chang, R.K., Jha, S.S., and Lee, C.H. (1968) Optical second harmonic generation in reflection from media with inversion symmetry. *Phys. Rev.*, **174**, 813–822.

7 Boyd, R.W. (2008) *Nonlinear Optics*, Academic Press.

8 Zernike, F. and Midwinter, J.E. (1973) *Applied Nonlinear Optics*, John Wiley & Sons, Inc., New York.

9 Guyot-Sionnest, P. and Shen, Y.R. (1988) Bulk contribution in surface second-harmonic generation. *Phys. Rev. B*, **38**, 7985–7989.

10 Heinz, T.F., Loy, M.M., and Thomson, W.A. (1985) Study of Si (111) surfaces by optical second-harmonic generation: reconstruction and surface phase transformation. *Phys. Rev. Lett.*, **54**, 63–66.

11 Tom, H.W.K., Heinz, T.F., and Shen, Y.R. (1983) Second-harmonic reflection from silicon surfaces and its relation to structural symmetry. *Phys. Rev. Lett.*, **51**, 1983–1986.

12 Epperlein, D., Dick, B., and Marowsky, G. (1987) Second harmonic generation in centro-symmetric media. *Appl. Phys. B*, **44**, 5–10.

13 Kulyuk, L.L., Shutov, D.A., Strumban, E.E., and Aktsipetrov, O.A. (1991) Second-harmonic generation by an SiO_2–Si interface: influence of the oxide layer. *J. Opt. Soc. Am. B*, **8**, 1766–1769.

14 Sipe, J.E., Moss, D.J., and van Driel, H.M. (1987) Phenomenological theory of optical second- and third-harmonic generation from cubic centrosymmetric crystals. *Phys. Rev. B*, **35**, 1129–1141.

15 Govorkov, S.V., Koroteev, N.I., Petrov, G.I., Shumay, I.L., and Yakovlev, V.V. (1990) Laser nonlinear-optical probing of Silicon/SiO_2 interfaces: surface stress formation and relaxation. *Appl. Phys. A*, **50**, 439–443.

16 Emelyanov, V.I., Koroteev, N.I., and Yakovlev, V.V. (1987) Second order nonlinear optical susceptibility introduced by inhomogeneous stress in crystals with inversion symmetry. *Opt. Spectrosc.*, **62**, 1188–1190.

17 Huang, J.Y. (1994) Probing inhomogeneous lattice deformation at interface of Si(111)/SiO_2 by optical second-harmonic reflection and Raman

spectroscopy. *Jpn. J. Appl. Phys.*, **33**, 3878–3886.
18 Lee, C.H., Chang, R.K., and Bloembergen, N. (1967) Nonlinear electroreflectance in silicon and silver. *Phys. Rev. Lett.*, **18**, 167–170.
19 Mizrahi, V. and Sipe, J.E. (1987) Phenomenological treatment of surface second-harmonic generation. *J. Opt. Soc. Am. B*, **3**, 660–667.
20 Lüpke, G., Bottomley, D.J., and van Driel, H.M. (1994) Second- and third-harmonic generation from cubic centrosymmetric crystals with vicinal faces: phenomenological theory and experiment. *J. Opt. Soc. Am. B*, **11**, 33–44.
21 Bottomley, D.J., Lüpke, G., Meyer, C., and Makita, Y. (1995) Exact separation of surface and bulk contributions to anisotropic second-harmonic generation from cubic centrosymmetric media. *Opt. Lett.*, **20**, 453–455.
22 Abdullaev, A.Y., Govorkov, S.V., Kashkarov, P.K., Koroteev, N.I., Petrov, G.I., and Shumay, I.L. (1987) Nonlinear optical probing of Si lattice deformation during thermal oxidation. *Sov. Phys. Solid State*, **27**, 1898–1892.
23 Friedman, L. and Soref, R.A. (1987) Second-order optical susceptibilities of strained GeSi/Si superlattice. *J. Appl. Phys.*, **61**, 2342–2346.
24 Govorkov, S.V., Emel'yanov, V.I., Koroteev, N.I., Petrov, G.I., Shumay, I.L., and Yakovlev, V.V. (1989) Inhomogeneous deformation of silicon surface layers probed by second-harmonic generation in reflection. *J. Opt. Soc. Am. B*, **6**, 1117–1124.
25 Phillips, J.C. and Van Vechten, J.A. (1993.) Nonlinear optical susceptibilities of covalent crystals. *Phys. Rev.*, **183**, 709–711.
26 Lyubchanskii, I.L., Dadoenkova, N.N., Lyubchanskii, M.I., Rasing, T., Jeong, J.-W., and Shin, S.-C. (2000) Second-harmonic generation from realistic film-substrate interfaces: the effects of strain. *Appl. Phys. Lett.*, **76**, 709–711.
27 Jeong, J.W., Shin, S.-C., Lyubchanskii, I.L., and Varyukhin, V.N. (1995) Strain-induced three-photon effects. *Phys. Rev. B*, **62**, 453–455.
28 Armstrong, J.A., Bloembergen, N., Ducuing, J., and Pershan, P.S. (1962) Interactions between light waves in a nonlinear dielectric. *Phys. Rev.*, **127**, 1918–1938.
29 Lifshitz, E.M., Kosevich, A.M., Kitaevskii, L.P., and Landau, L.D. (2007) *Theory of Elasticity*, Elsevier.
30 Kobeda, E. and Irene, E.A. (1989) *In situ* stress measurements during thermal oxidation of silicon. *J. Vac. Sci. Technol. B*, **7**, 163–166.
31 An, Y.Q. (2003) Spectroscopic studies of optical second-harmonic generation from Si(001) surfaces. PhD thesis. University of Colorado.
32 Cundiff, S.T., Knox, W.H., Baumann, F.H., Evans-Lutterodt, K.W., Tang, M.T., Green, M.L., and van Driel, H.M. (1997) Si/SiO_2 interface roughness: comparison between surface second harmonic generation and X-ray scattering. *Appl. Phys. Lett*, **70**, 1414–1416.
33 Daum, W., Krause, H.-J., Reichel, U., and Ibach, H. (1993) Identification of strained silicon layers at $Si–SiO_2$ interfaces and clean Si surfaces by nonlinear optical spectroscopy. *Phys. Rev. Lett.*, **71**, 1234–1237.
34 Dolgova, T.V., Bessonov, V.O., Maidykovsky, A.I., and Aktsipetrov, O.A. (2006) Surface-strain-induced second harmonic in silicon. Proceedings of Frontiers in Optics, p. JWD68.
35 An, Y.Q. and Cundiff, S.T. (2002) Bulk and surface contributions to resonant second-harmonic generation from Si(001) surfaces. *Appl. Phys. Lett.*, **81**, 5174–5176.
36 Rim, K., Anderson, R., Boyd, D., Cardone, F., Chan, K., Chen, H., Christiansen, S., Chu, J., Jenkins, K., Kanarsky, T., Koester, S., Lee, B.H., Lee, K., Mazzeo, V., Mocuta, A., Mooney, P.M., Oldiges, P., Ott, J., Ronsheim, P., Roy, R., Steegen, A., Yang, M., Zhu, H., Ieong, M., and Wong, H.-S.P. (2003) Strained Si CMOS (SS CMOS) technology: opportunities and challenges. *Solid State Electron.*, **47**, 1133–1139.
37 Jacobsen, R.S., Andersen, K.N., Borel, P.I., Fage-Pedersen, J., Frandsen, L.H., Hansen, O., Kristensen, M., Lavrinenko,

A.V., Moulin, G., Ou, H., Peucheret, C., Zsigri, B., and Bjarklev, A. (2006) Strained silicon as a new electro-optic material. *Nature*, **441**, 199–202.

38 Fage-Pedersen, J., Frandsen, L.H., Lavrinenko, A.V., and Borel, P.I. (2006) A linear electro-optic effect in silicon, induced by use of strain. Proceedings of 3rd IEEE International Conference on Group IV Photonics, pp. 37–39.

39 Xu, D.-X., Cheben, P., Dalacu, D., Delage, A., Janz, S., Lamontagne, B., Picard, M.-J., and Ye, W.N. (2000) Eliminating the birefringence in silicon-on-insulator ridge waveguides by use of cladding stress. *Opt. Lett.*, **29**, 2384–2386.

40 Tsia, K.K., Fathpour, S., and Jalali, B. (1993) Electrical control of parametric processes in silicon waveguides. *Opt. Express*, **16**, 9838–9843.

41 Tsia, K.K., Fathpour, S., and Jalali, B. (2008) Electrical tuning of birefringence in silicon waveguides. *Appl. Phys. Lett.*, **92**, 061109.

42 Baehr-Jones, T. and Hochberg, M. (2009) Slot machine. *Nat. Photonics*, **3**, 193–194.

43 Saleh, B.E.A. and Teich, M.C. (1991) *Fundamentals of Photonics*, John Wiley & Sons, Inc., New York.